The October 2024 Extreme Precipitation Event over Valencia: Storyline Attribution of the Synoptic-Scale Thermodynamic Drivers

Diego A. Campos[1,2], Katherine Grayson[1], Ramiro I. Saurral[1,3,4,5], Sebastian Beyer[6], Amal John[6], Matías Olmo[1], Francisco Doblas-Reyes[1,7]

5   [1]Barcelona Supercomputing Center, Barcelona, Spain
[2]Facultat de Física, Universitat de Barcelona, Barcelona, Spain
[3]CONICET-Universidad de Buenos Aires. Centro de Investigaciones del Mar y la Atmósfera (CIMA), Buenos Aires, Argentina
[4]Faculdad de Ciencias Exactas y Naturales, Departamento de Ciencias de la Atmósfera y los Océanos, Universidad de
10   Buenos Aires, Buenos Aires, Argentina
[5]CNRS-IRD-CONICET-UBA. Instituto Franco-Argentino para el Estudio del Clima y sus Impactos (IRL 3351 IFAECI), Buenos Aires, Argentina
[6]Alfred-Wegener-Institut, Helmholtz-Zentrum für Polar- und Meeresforschung (AWI), Bremerhaven, Germany
[7]Institució Catalana de Recerca i Estudis Avançats, Barcelona, Spain

15   *Correspondence to*: Diego A. Campos (diego.campos@bsc.es)

Abstract. In late October 2024, the western Mediterranean (WMed) region experienced an extreme precipitation event (EPE) centred over Valencia, southeastern Spain, associated with a quasi-stationary cut-off low (COL), producing record rainfall, flash floods, and severe societal impacts. The COL generated an atmospheric-river-like moisture plume from northwestern Africa, while additional moisture originated from the warm Mediterranean Sea. Interaction with regional 20 orography created a highly unstable environment, favouring deep convection and intense local rainfall. To assess the influence of anthropogenic climate change, we analyse high-resolution (~9 km) storyline simulations from the European Union's Destination Earth initiative, using the coupled IFS-FESOM model spectrally nudged with ERA5. Two climate scenarios are compared: Factual (present-day) and Counterfactual (~1950), isolating thermodynamic responses while keeping large-scale circulation fixed. Long-term IFS-FESOM and ERA5 datasets provide a climatological reference for 25 event extremeness. Results show that the synoptic configuration alone was sufficient to produce extreme rainfall, but human-induced warming substantially enhanced its magnitude. Moisture content and transport increased by 18–24%, convective instability (CAPE) by ~25%, and precipitation over Valencia increased by ~20% in the Factual scenario. Sea surface temperatures in the Western Mediterranean were ~2°C warmer, amplifying evaporation. Peak precipitation rates exhibited nonlinear amplification, on 29 October were about 36% higher in the Factual scenario, exceeding the Clausius–Clapeyron 30 (CC) scaling expected from the mean warming between scenarios. These findings indicate that anthropogenic warming can intensify EPEs in the WMed even when synoptic drivers alone would generate extreme rainfall, highlighting thermodynamic amplification as a key mechanism in Mediterranean flood events. High-resolution, physically consistent storyline simulations offer a robust framework for event-based attribution and improve understanding of future climate risks in vulnerable coastal regions.

35 **1 Introduction**

The western Mediterranean (WMed) region has been identified as a prominent climate change hotspot due to its accelerated warming and a decline in mean precipitation (Campos et al., 2025a; Campos et al., 2025b; Cos et al., 2022; Lionello & Scarascia, 2020; Tuel & Eltahir, 2020). This area is particularly vulnerable to the impacts of climate change, with both observed and projected increases in extreme precipitation events (EPEs; Olmo et al., 2025; Ribes et al., 2019; Tramblay &
40 Somot, 2018; Zittis et al., 2021). In the WMed, EPEs represent one of the most damaging weather phenomena, often responsible for severe floods, landslides, and infrastructure losses. EPE's impacts are particularly severe in densely populated coastal zones and mountainous cities along the Mediterranean Sea, where exposure to flood risk has increased as urban areas expand (Cánovas-García & Vargas Molina, 2025; Cortès et al., 2018). In these often mountainous regions, the orographic uplift enhances convective processes, especially during late summer and early autumn, when cold upper-level air
45 interacts with the warm Mediterranean Sea, fuelling intense rainfall (e.g., Insua-Costa et al., 2019; Terray & Bador, 2025). Understanding these events is therefore critical to both advancing climate research and developing effective adaptation and mitigation strategies under a rapidly changing climate (Gimeno et al., 2022; Llasat, 2024).

In late October 2024, the southeastern Iberian Peninsula experienced an episode of exceptionally heavy rainfall. The
50 Valencia region was the most severely affected, recording unprecedented precipitation that triggered widespread, devastating flooding (Llasat, 2024). Some weather stations in the area measured more than 600 mm of rain on October 29th—an amount exceeding the region's average annual total within just a few hours (AEMET, 2024). The event was also accompanied by other severe weather phenomena, including large hail and tornadoes (AEMET, 2024). Overall, the disaster resulted in more than 200 fatalities and caused billions of euros in damages (Llasat, 2024; Martin-Moreno et al., 2025).

55

At the synoptic scale, the event was associated with a quasi-stationary cut-off low (COL) system positioned over the southwestern sector of the WMed. COLs, defined as upper-level low-pressure systems isolated from the main westerly flow, are relatively common features in the synoptic climatology of the region (Gimeno et al., 2007; Nieto et al., 2008). This event is popularly known as the 'DANA of Valencia', given the acronym for COLs in Spain (Depresión Aislada en Niveles Altos).
60 COLs have been widely recognised as key precursors of EPEs in the WMed (Nieto Ferreira, 2021; Porcù et al., 2007; Saurral et al., 2025; Vicente-Serrano et al., 2025) and in other regions with Mediterranean climate worldwide (e.g., Barrett et al., 2016; Valenzuela et al., 2022), primarily due to the deep convection generated by the interaction between the cold air associated with the upper-level low and the warm, moist air beneath it (Insua-Costa et al., 2019). This mechanism is strongly conditioned by the amount and transport of environmental moisture, which have been identified as key factors controlling
65 the intensity of precipitation associated with COLs (Bozkurt et al., 2016; Muñoz & Schultz, 2021; Tsuji & Takayabu, 2019). COLs, which are projected to become more frequent under future climate conditions (Mishra et al., 2025), are therefore particularly relevant in the context of a warming world. As global temperatures rise, atmospheric moisture availability

increases (Held & Soden, 2006), enhancing the potential for intense precipitation and flooding events (Gründemann et al., 2022; Xiong & Yang, 2024; Zittis et al., 2021) in accordance with the Clausius–Clapeyron (CC) relationship. However, several studies have reported deviations from the expected CC scaling between temperature and precipitation (Drobinski et al., 2018; Pall et al., 2011, and references therein), underscoring the importance of event-based attribution analyses to better understand the role of climate change in shaping individual extreme events. In this regard, preliminary studies focusing on the Valencia EPE have already indicated that anthropogenic warming significantly contributed to the exceptional intensity of the episode (Barriopedro et al., 2025; Calvo-Sancho et al., 2025; Faranda et al., 2024). Nevertheless, these studies provide only a partial understanding of the event, as several key processes underlying its development and intensity have yet to be investigated.

The event-based storyline approach (Shepherd et al., 2018) provides a framework for assessing the influence of climate change on EPEs. Within this framework, the focus lies on how thermodynamic changes in the background climate modify the magnitude and characteristics of a particular event, while keeping the large-scale dynamics fixed (Zhuo et al., 2025). Among the different modelling strategies used to construct event-based storylines, the spectral nudging technique has become particularly prominent in both regional and global climate modelling (Feser & Shepherd, 2025; Van Garderen et al., 2021). Spectral nudging (e.g., Von Storch et al., 2000) constrains the simulated atmosphere to closely follow the observed large-scale circulation during a given event, enabling the reproduction of the same meteorological situation under different levels of global warming. This approach allows isolating and quantifying the thermodynamic component of anthropogenic climate change associated with a specific event (Sánchez-Benítez et al., 2022; Van Garderen & Mindlin, 2022; Zhuo et al., 2025). Beyond its methodological robustness, the storyline framework also facilitates a more integrated understanding of climate change by linking the physical aspects of extreme events with their societal impacts, thereby making climate evolution more tangible and actionable (Baulenas et al., 2023).

In this paper, we investigate the role of climate change in the synoptic environment during the Valencia EPE of October 2024, focusing on moisture content, moisture transport, and atmospheric instability that lead to the extreme precipitation. We employ global km-scale (Hewitt et al., 2022; Schär et al., 2020) and spectrally-nudged storylines under both a Factual (present-day) and a Counterfactual (pre-industrial) climate (John et al., 2024). The simulations were performed within the framework of the European Union's Destination Earth initiative, which is a pioneer coordinated effort to implement Earth system's Digital Twins for climate adaptation (DestinE ClimateDT; Doblas-Reyes et al., 2025; Hoffmann et al., 2023; Wedi et al., 2022), using the coupled atmosphere–ocean model IFS-FESOM (Rackow et al., 2025) nudged with ERA5 reanalysis data (Hersbach et al., 2020). The remainder of this paper is structured into four main sections. Section 2 describes the data and methods used in the study. Section 3 presents the analysis results. Finally, in Section 4, the main results are discussed, and questions for future studies are raised.

2 Data and Methods

2.1 Model data

In this work, we analyse the spectrally-nudged storyline simulations conducted with the coupled global climate model IFS-
FESOM from the DestinE ClimateDT initiative. This modelling framework couples the Integrated Forecasting System (IFS,
cycle 48r1; ECMWF, 2023), developed by ECMWF, for the atmosphere, land, and waves, with the Finite volumE Sea Ice-
Ocean Model (FESOM2, version 2.5) from the Alfred Wegener Institute. The setup used corresponds to the ClimateDT
configuration (Rackow et al., 2025). The atmospheric component has a horizontal resolution of roughly 9 km (TCo1279
spectral resolution) with 137 vertical levels. The ocean component has 70 vertical levels and uses a horizontal resolution
(unstructured NG5 mesh) that smoothly transitions from about 12 km in the tropics to 4.5 km in dynamically active regions
and polar areas (Danilov et al., 2017; Scholz et al., 2019).

The spectral nudging used to constrain the large-scale circulation towards the observations in the simulations was made
following the methodology of Sánchez-Benítez et al. (2022). This approach relaxes large-scale vorticity and divergence in
the model towards ERA5 reanalysis data between 700 and 100 hPa up to wavenumber T60. Additionally, a 1-hour e-folding
was employed to maintain consistency with the observed large-scale flow, while allowing the model to simulate small-scale
processes freely (John et al., 2024). In this way, the large-scale flow above 700 hPa remains consistent with ERA5, allowing
changes in the nudged simulations to be mainly attributed to thermodynamic features and small-scale dynamics.

Two climate scenarios are considered in this study: Factual (present-day climate) and Counterfactual (cooler climate). These
scenarios were driven by the same spectrally-nudged large-scale circulation and initial atmospheric conditions (01-01-2017
ERA5) and were run for the period 2017-2024. They do differ in their boundary and ocean initial conditions, allowing the
evaluation of how identical meteorological events evolve under contrasting climate states:

- Counterfactual (cooler) – representing a pre-industrial-like state based on 1950 boundary conditions with CMIP6-
  historical forcing. In this experiment, the forcing is held fixed at its 1950 values for the entire 2017-2024 simulation
  period.
- Factual (present-day) – representing current conditions (2017–2024) forced with the SSP3-7.0 scenario. In this case,
  the external forcing is transient and evolves year by year.

For each simulation, a five-year ocean spin-up was performed using stand-alone FESOM2 integrations (1945–1949 for the
Counterfactual and 2012–2016 for the Factual). For details, please refer to John et al. (2024).

To ensure robustness in the differences between the Factual and Counterfactual experiments, we use four additional
ensemble members for each variable, generated using the same methodology described above and complementing the main

run. These experimental members branch from the main simulations using the July 2024 restart files. To introduce small
135   perturbations, nudging is temporarily switched off for a different number of days in each member: one day for the first
member, two for the second, three for the third, and so on, before being reactivated. This procedure allows the model to
evolve freely for a short period, creating slightly different atmospheric states that stabilise during the subsequent nudged
period and provide a representation of internal variability. The limited ensemble size is primarily due to the high
computational cost of conducting global km-scale simulations.

140   **2.2 Synoptic variables**

For our analyses, we use hourly model output from 00 UTC on 24 October 2024 to 23Z on 31 October 2024, covering the
domain 35°W–20°E and 10–60°N. The variables considered include the zonal and meridional wind components (u, v),
vertical velocity (ω), specific humidity (q), and geopotential height, at the following pressure levels: 1000, 925, 850, 700,
600, 500, 400, 300, 250, 150, 100, and 70 hPa. Additionally, we analysed precipitation rate, mean sea level pressure
145   (MSLP), 2-meter air temperature, total column water vapour (TCWV), sea surface temperature (SST), and evaporation.
From these variables, we further derived the Most Unstable Convective Available Potential Energy (CAPE) using the MetPy
Python library (May et al., 2022) and Integrated Water Vapour Transport (IVT) using Eq. (1),

$$IVT = \frac{1}{g} \int_{1000\ hPa}^{300\ hPa} \boldsymbol{V} q \, dp, \tag{1}$$

where g is the acceleration of gravity, $\boldsymbol{V} = (u, v)$ is the wind components, and dp is the depth of atmospheric layers in terms
150   of pressure.

To provide observational and reanalysis context, we also obtained the same set of atmospheric variables from ERA5 via the
Copernicus Climate Data Store (Copernicus Climate Change Service, 2018). Daily SSTs were taken from the NOAA
OISSTv2 database (Huang et al., 2021). Daily precipitation was derived from the Multi-Source Weighted-Ensemble
155   Precipitation (MSWEP, Beck et al., 2019) and E-OBS (Cornes et al., 2018) datasets, as well as from ground-based
observations provided by the Spanish Meteorological Agency (Agencia Estatal de Meteorología, AEMET) and the
Valencian Meteorological Association (Associació Valenciana de Meteorologia, AVAMET). The full list of stations is
provided in Supplementary Table 1.

160   To analyse the pathways of air parcels reaching Valencia on the day of the event, we used the online version of the
HYSPLIT model (Stein et al., 2015), available through the NOAA Air Resources Laboratory website. An analysis of 72-
hour backward trajectories was performed for air parcels arriving at Valencia (39.47°N, 0.37°E) at 12Z on 29 October, at
four different arrival heights: 250, 1000, 2000, and 3000 m above sea level (ASL). The trajectories were computed using

data from the NCEP Global Data Assimilation System (GDAS). For each arrival height, an ensemble of 27 members was
generated to account for trajectory uncertainty.

2.3 Long-term simulation

To assess the magnitude and uniqueness of the event, we placed it into a long-term climatological context. For this purpose,
we used an extended IFS-FESOM reference climate simulation (hereafter referred to as IFS-FESOM) covering the period
1950-2014, obtained from the European Eddy RIch Earth System Models (EERIE) project (Ghosh et al., 2025). Unlike the
spectrally-nudged simulations described above, this experiment was performed without spectral nudging, allowing the model
to freely evolve. Apart from this difference, all other aspects of the experimental setup remained identical, including the
atmospheric and oceanic components, parameterisations, and horizontal and vertical resolutions (Rackow et al., 2025). This
consistency allows the IFS-FESOM simulation to be used as a physically coherent climatology to contextualise the storyline
scenarios. To reduce storage and computational costs, the output data were regridded onto a regular 0.25°x0.25° grid.

For the present analysis, daily values of selected key variables during the Valencia EPE were compared with their
corresponding October-November daily values from the 1950-2014 IFS-FESOM simulation, as well as from ERA5 over the
same reference period. Percentile-based thresholds (e.g., 5th or 95th percentiles) were calculated from the October–
November daily values over the reference period, separately for IFS-FESOM and ERA5. This percentile-based comparison
with a long reference simulation follows the climatological framing used in Van Garderen et al. (2021) to contextualise event
extremeness. In our case, we use a bi-monthly climatology because including September (i.e., using the SON season) would
incorporate markedly warmer and drier conditions that might not be representative of the late-October environment in which
the event developed (e.g., Figure 3 in Campos et al., 2025a). For precipitation, the maximum daily precipitation index
(Rx1day) was computed as the highest daily precipitation amount within each month, following the Expert Team on Climate
Change Detection and Indices (ETCCDI; Zhang et al., 2011) definition, over Valencia. This Rx1day was then compared
with the 95th percentile from the same reference period.

2.4 Event attribution

To assess the influence of climate change on the variables that influenced the Valencia EPE, we compared the Factual and
Counterfactual scenarios by subtracting the latter from the former. We then calculated the relative changes following Eq. (2),
which quantifies the percentage difference between the Factual (present-climate) and Counterfactual (colder-climate) values,
normalised by the Counterfactual state.

$$Relative\ change = \frac{Factual - Counterfactual}{Counterfactual} \times 100 \qquad (2)$$

To assess whether the differences between scenarios lie outside the range of internal variability, we applied a signal-to-noise approach following the methodology of Van Garderen et al. (2021). The method uses all possible pairwise combinations of
195 ensemble members to compute differences both within and between scenarios. The inter-scenario differences (Factual – Counterfactual) represent the signal, while the intra-scenario differences (Factual – Factual and Counterfactual – Counterfactual) represent the noise. Following Van Garderen et al. (2021), a significant signal-to-noise ratio is identified when the median of the signal distribution lies outside the inter-quartile range of the noise. This criterion directly follows the approach used in Van Garderen et al. (2021), where detectability is established when the central value of the signal exceeds
200 the spread associated with internal variability.

3 Results

3.1 Event description and model validation

The devastating EPE in Valencia (represented by the red dot in Fig. 1a) occurred on 29 October 2024. In this section, the
205 event is described based on the Factual simulation from the DestinE ClimateDT model, which provides the main reference for the analysis. ERA5 is included for intercomparison purposes and is shown in the Supplementary Material.
On this day, in the Factual scenario (Fig. 1), an upper-level COL is located over the southwestern Iberian Peninsula, centred near 35°N, 5°W. The system is fully separated from the main westerly flow, as indicated by the maximum wind speeds observed along the southern flank of the COL, which is isolated from the jet stream. The COL is flanked by two ridges, one
210 to the northwest and another to the southeast (Fig. 1a). On the same day, the system exhibited a quasi-barotropic structure, with the upper-level low nearly in phase with the 700 hPa low (Fig. 1c) and its corresponding surface projection (Fig. 1d). A similar vertical alignment is observed for the adjacent ridges, indicating a coherent barotropic configuration throughout the troposphere. This configuration persisted for several days (not shown), with the COL drifting slightly southwestward from the central Iberian Peninsula between 27 and 29 October, thereby maintaining its quasi-stationary character. This persistent
215 evolution is consistent with that found in ERA5, as expected given the spectral nudging applied in the simulation (Fig. S1 in the Supplement).

Over the Mediterranean coast of Spain, TCWV (shaded colours in Fig. 1b) exceeds 30 kg m^{-2}, enhanced by a plume of moisture transported from the subtropical Atlantic across northwestern Africa in an atmospheric-river-like (AR-like)
220 structure. This plume, located along the eastern flank of the COL, exhibits local IVT magnitudes exceeding 500 kg m^{-1} s^{-1} (Fig. 1b). The moisture flux reaches almost perpendicularly on the Valencian coast (see Fig. S2 in the Supplement for the model's topography), favouring moisture convergence and orographic lifting as the low-level flow interacts with the local topography (Fig. 1c). This moist environment off the Valencian coast is also unstable, with convective available potential energy (CAPE) values exceeding 1500 J kg^{-1} (Fig. 1d).

225

The synoptic configuration in the Factual scenario shows good agreement with ERA5, not only for the nudged dynamical fields, such as geopotential height, but also for thermodynamic variables like TCWV (Fig. S3 in the Supplement). The main discrepancy arises from an underestimation of CAPE over land in the Factual scenario compared to ERA5. This difference might be related to the coarser vertical resolution used to compute CAPE in the simulation (11 levels in the Factual scenario versus 27 levels in ERA5).

230
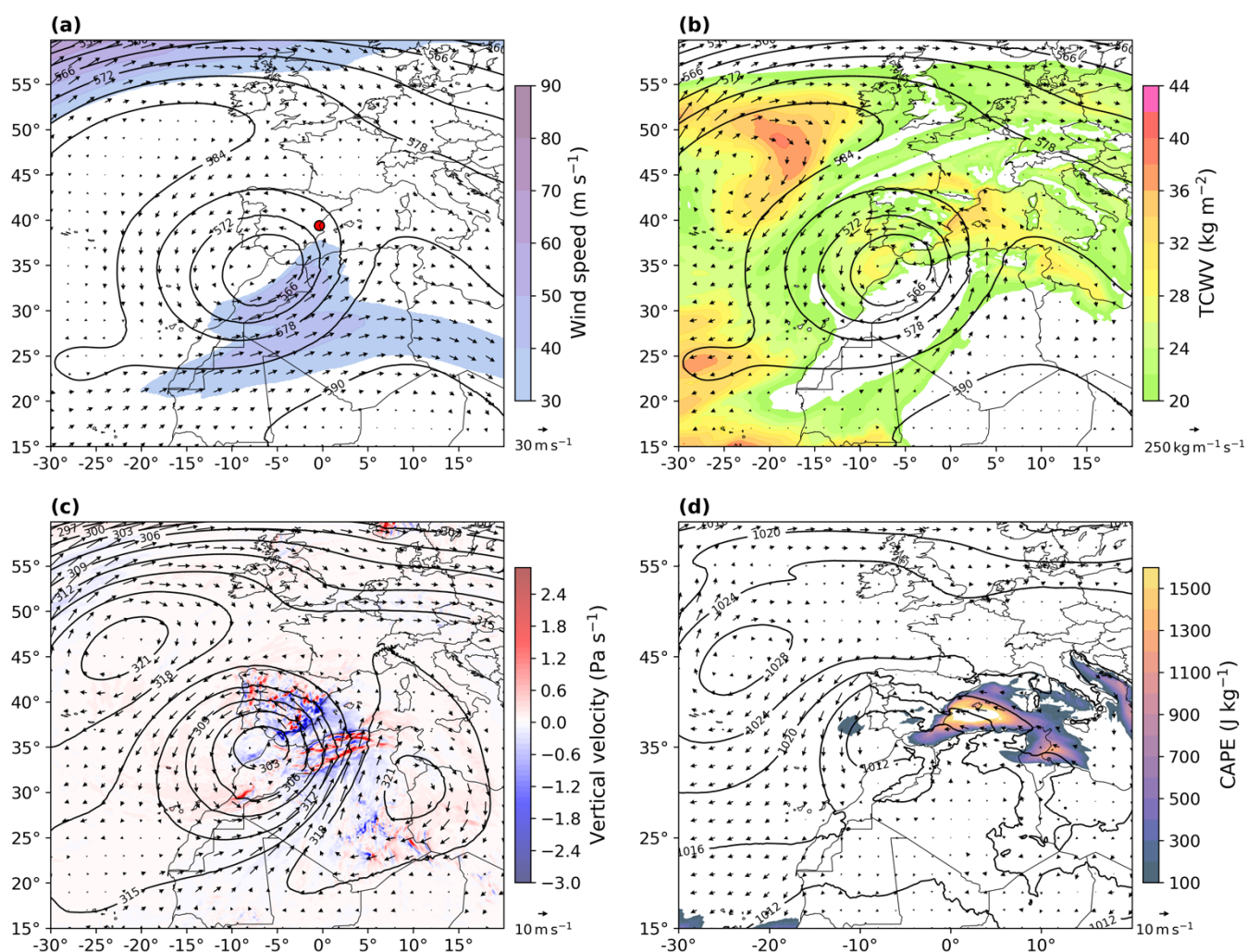
Figure 1: Daily composite for the 29 October 2024 from the Factual scenario for (a) 500-hPa geopotential height (contours, dam), 300-hPa wind (arrows, m s⁻¹) and 300-hPa wind speed (colours, m s-1), (b) 500-hPa geopotential height (contours, dam), integrated water vapour transport (IVT, arrows, kg m⁻¹ s⁻¹) and total column water vapour (TCWV, colours, kg m⁻²), (c) 700-hPa geopotential height (contours, dam), 700-hPa wind (arrows, m s⁻¹) and 700-hPa vertical velocity (colours, Pa s⁻¹), and (d) mean sea level pressure (MSLP, contours, hPa), 1000-hPa wind (arrows, m s⁻¹) and convective available potential energy (CAPE, colours, J kg⁻¹). The red dot on (a) shows the approximate location of Valencia.

235

240   Two main air parcel pathways can be identified reaching the Valencia area on the 29th. The first pathway, associated with the AR-like structure, originates over the subtropical Atlantic, crosses northwestern Africa at mid-tropospheric levels (approximately 2000–3000 m ASL), and arrives over Valencia at a similar altitude. In contrast, the second pathway travels at low levels (around 500 m ASL) across the Mediterranean Sea, reaching Valencia near the surface (Fig. 2a). The relatively warm SSTs over the Mediterranean (around 24 °C during the week of the event, Fig. 2a) favour the high values of TCWV

245   and CAPE observed in the region (Fig. 1b-d). To further investigate the contribution of these two moisture pathways to the precipitation in Valencia, and how they differ across climate scenarios, we define two regions: the Northwestern Africa region (NWA; 33.45°-35.45°N; 0.20°W-4.50°E) and the Mediterranean region (MED; 37.05°-41.05°N; 6.50°-8.50°E), as shown in red boxes in Fig. 2a.

250   The spatial precipitation pattern on 29 October in the Factual scenario is shown in Fig. 2b. A broad area over southern Iberia experiences rainfall during the day, with the highest amounts concentrated over the Valencia region, where a local maximum of approximately 180 mm is simulated. This pattern closely resembles that from ERA5, although the higher horizontal resolution of the Factual simulation provides greater spatial detail, particularly in capturing the influence of topography on precipitation. In contrast, E-OBS and MSWEP display a more homogeneous spatial distribution (Fig. S4 in the Supplement).

255   Despite the realistic spatial distribution, the Factual simulation underestimates total precipitation compared to local ground stations in the Valencia region, which recorded more than 600 mm in 24 hours (Table S1 and Fig. S5 in the Supplement). Therefore, in this study, we focus on the synoptic environment and the regional characteristics of precipitation over Valencia, and define the Valencia box, VAL (38.25°-40.50°N; 1.75°W-0.25°E, black box in Fig. 2c) for further analysis.

260   Between 24 and 31 October, the Valencia region (VAL) accumulated an average of approximately 100 mm of precipitation, with local maxima reaching around 200 mm. Most of this rainfall occurred on 29 October, when the highest precipitation rates were simulated, with mean values of about 2 mm h^{-1}, and local peaks exceeding 10 mm h^{-1} (Fig. 2c). The precipitation maximum on 29 October coincides with a period of enhanced atmospheric instability over VAL, characterised by mean CAPE values near 600 J kg^{-1}, local maxima close to 2000 J kg^{-1}, and a (negative) peak in vertical velocity at 700 hPa (Fig.

265   2d).

These precipitation and instability peaks are closely linked to the evolution of the IVT and TCWV over the region. The westward (negative) zonal component of the IVT over VAL gradually increases with time, reaching a maximum of about 400 kg m^{-1} s^{-1} on 29 October (Fig. 2e). At the same time, the northward (positive) meridional component (IVTy) over the

270   northwestern Africa region (NWA) also peaks near 400 kg m^{-1} s^{-1}, associated with the AR-like moisture plume (Fig. 2f). The biggest contribution from the Mediterranean region (MED) appears to occur one to two days earlier, when the IVT reaches its maximum with a southeasterly orientation (Fig. 2e-f). The maximum TCWV over VAL is observed on 29 October, with

values close to 30 kg m^{-2}, followed by a rapid decrease associated with the dissipation of the NWA moisture inflow and the peak in precipitation on the same day (Fig. 2g). In contrast, TCWV over the MED remains relatively steady through time,

275 suggesting it is mainly governed by local processes rather than remote moisture transport (Fig. 2g).
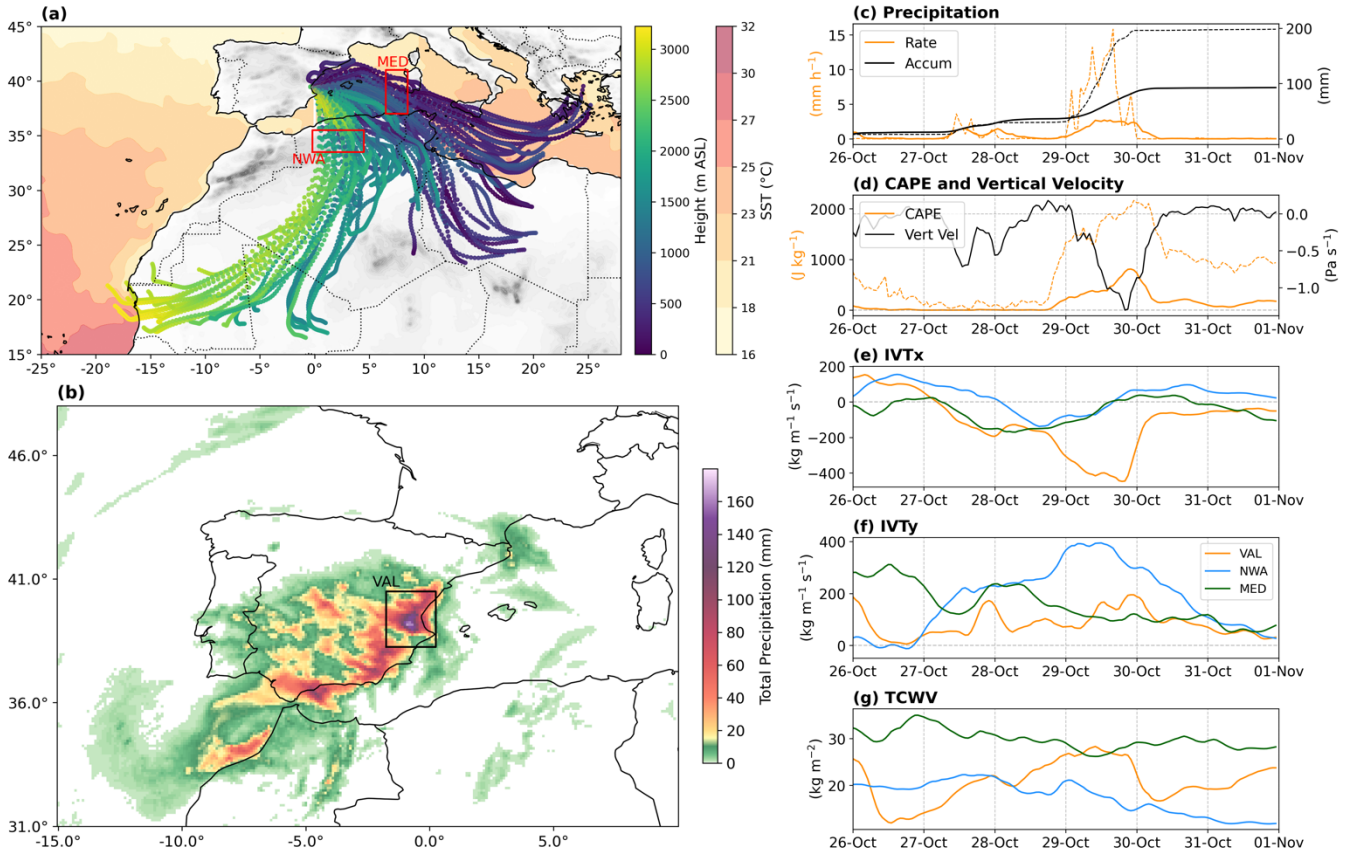
Figure 2: (a) 72-hour backward trajectories from the HYSPLIT model for air parcels arriving in Valencia at 12Z on 29 October, and 7-day mean (24-30 Oct) SSTs (°C) from NOAA OISSTv2. Red boxes indicate the Mediterranean (MED) and Northwestern

280 Africa (NWA) boxes. **(b)** 24-hour accumulated precipitation on 29 October from the Factual scenario, with the Valencia (VAL) box shown in black. **(c)** Hourly precipitation rate (orange) and accumulated precipitation (black) over the Valencia box. Solid lines indicate the box mean, and dashed lines indicate the grid cell with the highest accumulation. Accumulated precipitation is computed starting at 00 UTC on 24 October. **(d)** 700-hPa vertical velocity (black) and CAPE (orange) over the Valencia box. Solid lines show the box mean, and the orange dashed line indicates the highest hourly CAPE within the box. **(e)** Hourly mean zonal IVT

285 (IVTx) over VAL (orange), NWA (blue), and MED (green). **(f)** As in (e), but for meridional IVT (IVTy). **(g)** As in (f), but for TCWV.

3.2 Long-term perspective

We now analyse the key variables associated with the Valencia EPE, described in Section 3.1, within a climatological

290 context. For this purpose, we used the long IFS-FESOM simulation and ERA5 reanalysis over the 1950-2014 period as

reference datasets; ERA5 provides an observational reference, while the long IFS-FESOM run offers a model-consistent climatology for the storyline framework. The extremeness of the event was assessed using the maximum daily precipitation index (Rx1day) over the VAL region (Fig. 3a). During the Valencia EPE, the spatially averaged daily precipitation in the Factual scenario reached nearly 44 mm (red dashed line in Fig. 3a), exceeding the 95th percentile of the Rx1day distribution in the long IFS-FESOM simulation (~28 mm; thin light blue line in Fig. 3a). In statistical terms, this indicates that the Valencia EPE qualifies as an extreme event. A similar conclusion is obtained from ERA5, although in this case, the event magnitude exceeds the 95th percentile by a smaller margin than in the IFS-FESOM world (black and grey lines in Fig. 3a).

295
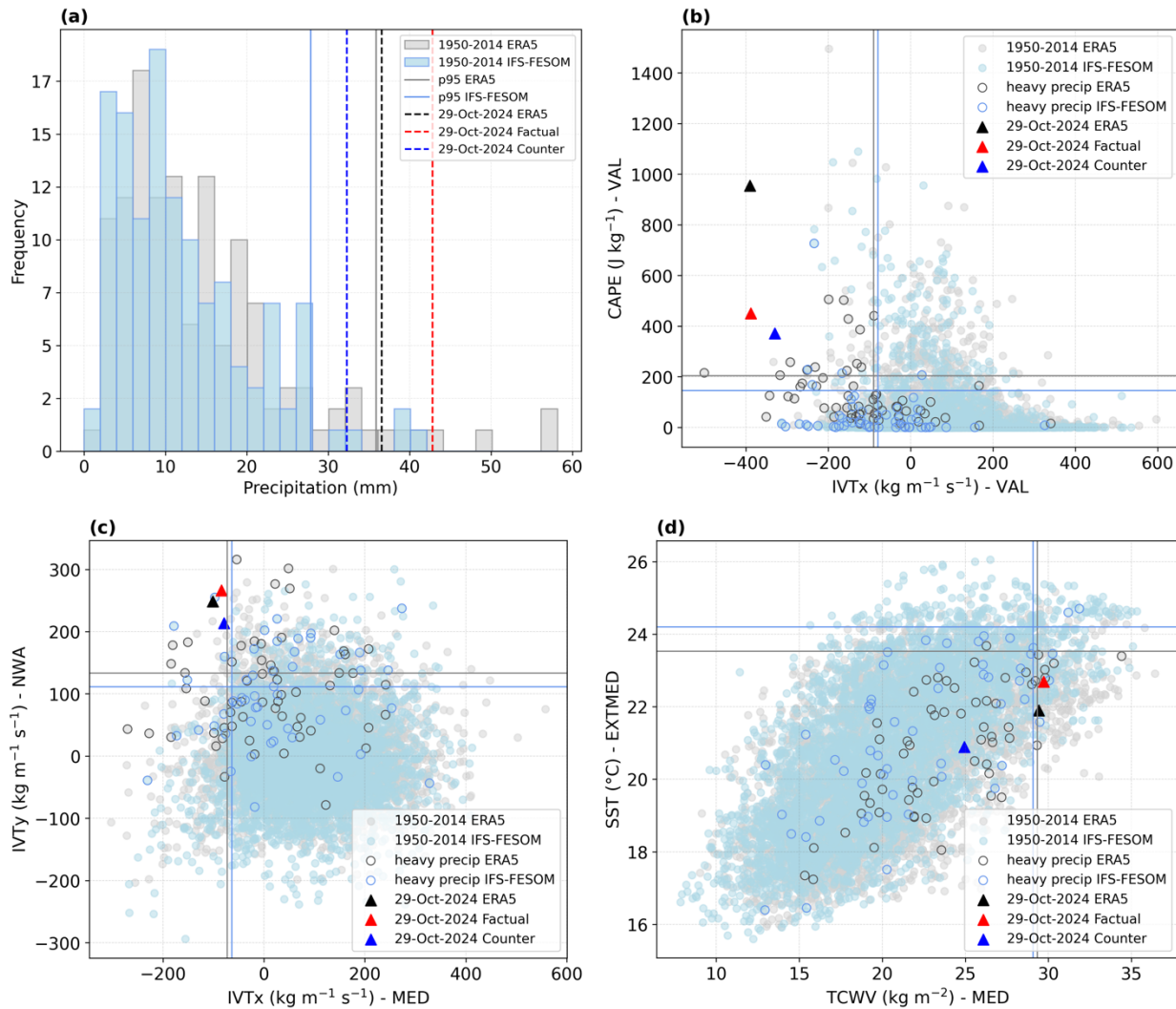
300 **Figure 3: (a) Distribution of maximum daily precipitation (Rx1day) in Valencia (VAL box) for October–November during 1950–2014 in ERA5 (light grey bars) and IFS-FESOM free run (light blue bars). (b) Daily mean IVTx and CAPE values spatially averaged over VAL for October–November during 1950–2014 in ERA5 (light grey circles) and IFS-FESOM (light blue circles). (c) As in (b), but for the 3-day mean IVTx values spatially averaged over the Mediterranean box (MED) and IVTy over northwestern**

Africa box (NWA). (d) As in (c), but for TCWV over MED and SST over an extended Mediterranean box (EXTMED; 36.5°–
305 **40.5°N; 0.0°–8.5°E). Thin vertical lines (light grey for ERA5, light blue for IFS-FESOM) indicate the 5th or 95th percentiles of the**
1950–2014 reference period, as appropriate. Dashed vertical lines in (a) and triangles in (b)–(d) denote the values on 29 October
for ERA5 (black) and for the Factual (red) and Counterfactual (blue) scenarios. Bordered circles in (b) indicate days with heavy
precipitation in VAL (defined as exceeding the 75th percentile). In (c) and (d), bordered circles indicate heavy-precipitation days
based on the last day of the 3-day period.

310

If we now apply this analysis as an approximation for a statistical attribution assessment, following a strategy similar to Van Garderen et al. (2021), we can compare the Factual and Counterfactual scenarios within a climatological context. For Rx1day in VAL, both scenarios exceed the 95th percentile, although the Counterfactual scenario exhibits a lower magnitude (see red and blue dashed lines in Fig. 3a). This suggests that the event would also have been extreme under a colder climate,
315 although less intense.

Following the same approach, but now focusing on a combination of variables associated with the extreme precipitation over VAL, we analysed the daily IVTx and CAPE spatially averaged over this region (Fig. 3b). On the day of the event, a situation characterised by high CAPE and strongly negative IVTx values is observed (black and red triangles in Fig. 3b).
320 Heavy precipitation events in VAL tend to occur under negative IVTx conditions, i.e., an easterly moisture flux from the Mediterranean Sea toward the region, which effectively transports humid air and contributes to convective development; however, CAPE does not appear to be a determining factor in these heavy precipitation events (bordered circles in Fig. 3b). On October 29, both variables exceeded their respective thresholds for statistical extremeness in both the ERA5 and IFS-FESOM datasets. Furthermore, both the Factual and Counterfactual scenarios exceed the 95th percentile, suggesting that the
325 intense zonal moisture flux and atmospheric instability observed on 29 October would have been considered extreme even in the absence of anthropogenic climate change (Fig. 3b).

In a similar way, we examine the extremeness of the moisture transport contributions from both NWA and MED. Because these regions are distant from VAL and the maximum IVT does not necessarily coincide with the day of heavy precipitation
330 there (see Fig. 2c-g), we use 3-day mean values for each variable. Figure 3c shows the 3-day mean IVTx over MED and IVTy over NWA. During the event, a strong positive IVTy over NWA, typically associated with heavy precipitation in VAL (see bordered circles in Fig. 3c), acted in combination with a strong negative IVTx over MED (Fig. 3c). Both variables reach extreme values, with those in the Factual scenario exceeding the thresholds derived from the long IFS-FESOM simulation, particularly for IVTy in NWA. The same result is obtained when using ERA5 data (Fig. 3c). For both variables, the
335 Counterfactual closely follows the Factual, with values remaining above the extreme threshold. This indicates that the moisture transport from the NWA and MED regions would also have been extreme in a colder climate (Fig. 3c).

The final set of variables examined from a long-term perspective are TCWV and SST over the Mediterranean Sea, given their relatively high values during the event (Fig. 2). For TCWV, we use the same MED region defined previously, while for

340 SST, we extend the MED box towards the Valencian coast, defining a new region: the extended Mediterranean box (EXTMED; 36.5°–40.5° N, 0.0° W–8.5° E, see Fig. 5a). This extension is made because, unlike in the analysis of moisture transport (where independence from the NWA box was needed), for SST and evaporation it is more relevant to encompass the marine area directly influencing the Valencia EPE. For both variables, 3-day mean values are used to place their magnitudes in the context of the 1950-2014 reference period, using both IFS-FESOM and ERA5 datasets (Fig. 3d). Most

345 heavy precipitation days in VAL do not exceed the 95th percentiles of TCWV and SST over the MED region, suggesting that these are not necessary conditions for extreme precipitation in VAL (see bordered circles in Fig. 3d). During the Valencia EPE of October 2024, TCWV over MED slightly exceeded the 95th percentile of the reference period in both the IFS-FESOM Factual scenario and ERA5, whereas SST over the EXTMED region did not (Fig. 3d). Interestingly, TCWV over MED is not extreme in the Counterfactual scenario, indicating that anthropogenic climate change substantially

350 contributed to the unusually high moisture content over MED during the 29 October event (Fig. 3d).

3.3 Factual–Counterfactual comparison

In this section, we analyse the role of climate change in shaping the synoptic environment and precipitation over Valencia during the event by comparing the Factual and Counterfactual scenarios. On 29 October, positive TCWV anomalies are

355 found across the entire domain, particularly within the AR-like moisture plume along the eastern flank of the COL circulation (Fig. 4). In this region, TCWV exceeds the Counterfactual values by more than 8 kg m^{-2}, and IVT increases by over 100 kg m^{-1} s^{-1} in the Factual scenario (Fig. 4a). We use here the geopotential height from the Factual scenario to depict the COL circulation, as no displacement in the COL position is found between scenarios due to the spectral nudging applied in the simulations. Nevertheless, we observe an increase in the COL 1000-500 hPa thickness from the Counterfactual to the

360 Factual scenario, consistent with the thermodynamic response to global warming (Fig. S6 and Fig. S7a in the Supplement; IPCC (2023); Santer et al. (2017)).

The enhancement of the AR-like moisture plume reaches its maximum on 29 October, with a southerly IVTy component over NWA increasing by about 100 kg m^{-1} s^{-1} (Fig. 4f). This intensified moisture transport subsequently impacts VAL,

365 where IVTx increases by nearly 70 kg m^{-1} s^{-1} (Fig. 4e), consistent with an increase in lower levels moisture availability (Fig. S7b in the Supplement). The IVT originating from the Mediterranean also strengthens in the Factual scenario, although to a lesser extent (Fig. 4e-f). In addition, the TCWV shows higher values across all regions due to climate change (Fig. 4g), indicating a general increase in moisture availability and transport.

370 This enhanced moisture supply has a direct effect on precipitation. On 29 October, precipitation increases markedly along the southeastern coast of Spain, with local maxima exceeding 40-50 mm over the VAL area (Fig. 4b). The higher precipitation rate throughout the day results in an additional 15-20 mm of rainfall accumulation over VAL during the event

(from 24 to 31 October, Fig. 4c). In parallel, atmospheric instability intensifies over the Mediterranean Sea, with local CAPE
differences reaching ~500 J kg^{-1} (Fig. 4b). Although the CAPE increase is less pronounced over land, values exceeding 100 J
375 kg^{-1} are observed over VAL on 29 October (Fig. 4d). The 700-hPa vertical velocity does not have a significant signal over
VAL (see the large spread among ensemble members in Fig. 4d), suggesting that the interaction between the flow and the
topography at lower levels remains similar across scenarios; however, at mid- to upper-tropospheric levels (600–300 hPa), a
tendency toward enhanced upward motion may be present (Fig.S7d in the Supplement).
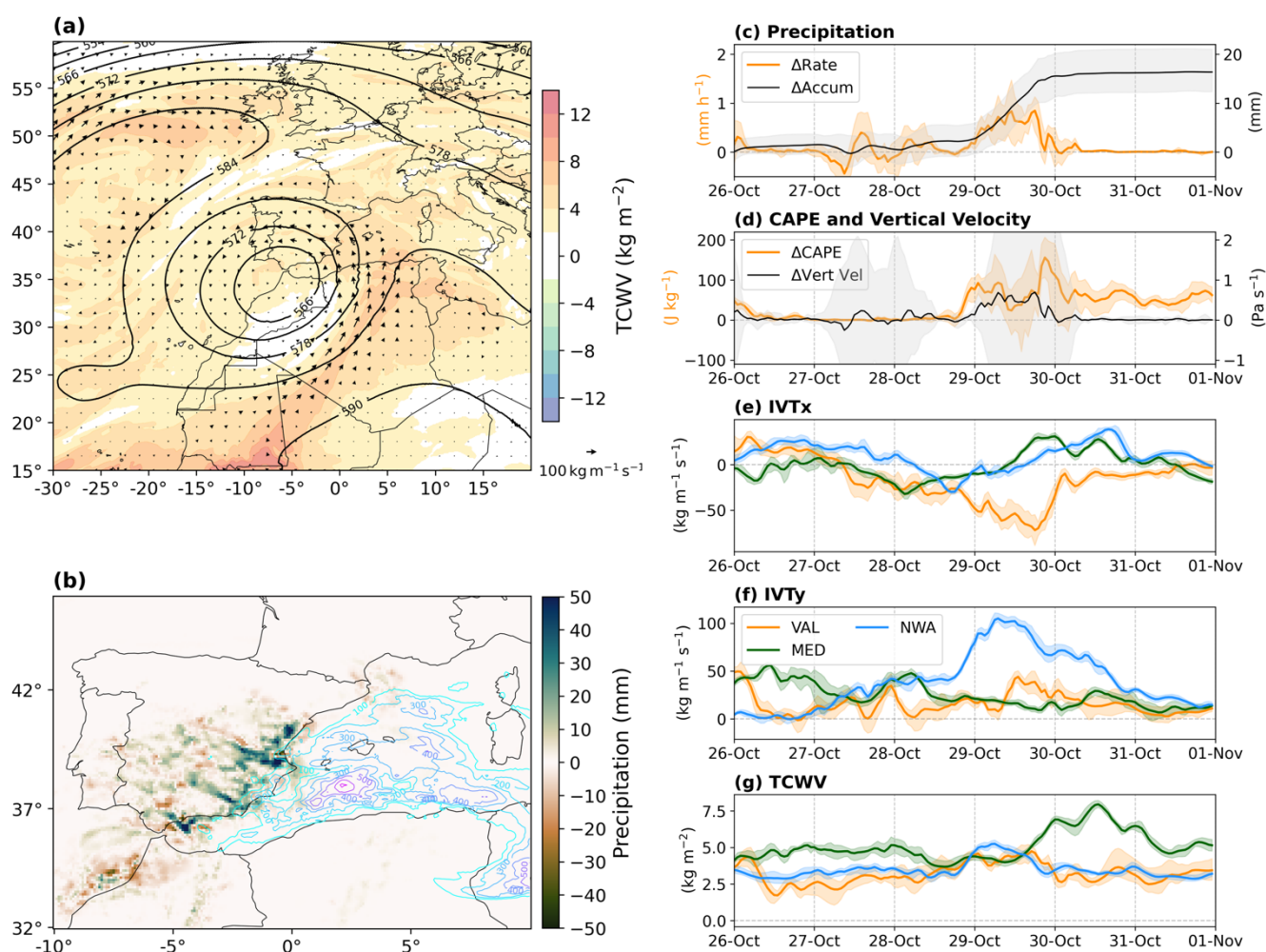
Figure 4: (a) Composite of mean daily differences (Factual – Counterfactual) on 29 October for IVT (arrows) and TCWV
(shading). Contours show the daily mean 500-hPa geopotential height (dam) in the Factual scenario (as in Figure 1a–b). (b) Mean
daily precipitation differences (shading, mm) and CAPE (contours, J kg^{-1}) on 29 October. For CAPE, only positive differences
above 100 J kg^{-1} are shown. (c) Hourly differences in precipitation rate (orange) and accumulated precipitation (black) over VAL.
385 Solid lines indicate the mean difference, and shading shows the minimum–maximum range. Accumulated precipitation is
computed starting at 00 UTC on 24 October. (d) As in (c), but for CAPE (orange) and 700-hPa vertical velocity (black). (e) As in
(d), but for hourly differences in IVTx over VAL (orange), NWA (blue), and MED (green). (f) As in (e), but for IVTy. (g) As in (f),
but for TCWV. The shading in panels (c) to (g) show the minimum-maximum range obtained using all the ensemble members.

Table 1 summarises the relative changes between the Factual and Counterfactual scenarios (Eq. 2) over the main regions and variables discussed above. Overall, the results indicate a coherent thermodynamic response to global warming, with consistent increases across all variables. The largest relative change is observed in precipitation rate over VAL, with a mean increase of 36% and a range of 14% to 57% across ensemble members. Accumulated precipitation over the 24-29 October period also increases by 20% on average. CAPE exhibits a substantial rise of about 25%, indicating enhanced atmospheric instability under warmer conditions. The moisture-related variables (TCWV and IVT) show more moderate but spatially consistent increases of 15-25% across the three regions, with the strongest relative changes in TCWV and IVT over NWA, reflecting the intensified subtropical moisture inflow that feeds the AR-like structure.

Table 1: Relative changes between the Factual and Counterfactual scenarios. *For precipitation rate and CAPE, only 29 October is considered. +Accumulated precipitation corresponds to the period from 24-29 October. The maximum–minimum range is estimated across all ensemble members.

Variable	Min (%)	Mean (%)	Max (%)
Precipitation rate (VAL)*	14	36	57
Accumulated precipitation (VAL)+	15	20	26
CAPE (VAL)*	6	25	42
IVT (VAL)	13	19	24
IVT (MED)	15	18	22
IVT (NWA)	23	25	28
TCWV (VAL)	15	18	21
TCWV (MED)	18	20	21
TCWV (NWA)	22	24	26

The SST over the Mediterranean Sea is higher in the Factual scenario, with an average increase of nearly 2°C and localised areas exceeding 3°C of increase (Fig. 5a). In the EXTMED region, the mean SST in the Factual scenario is about 22.5-23°C, compared to ~21°C in the Counterfactual scenario (Fig. 3d). These warmer SSTs are associated with enhanced evaporation, contributing to a moister environment near the coast of Valencia. In the days preceding 29 October, evaporation was notably higher in the Factual scenario than in the Counterfactual; however, on 29 October itself, no significant differences are observed (Fig. 5b). The relative change in evaporation is 5.5% (range: 4.5-6%). These findings suggest that climate change may have played a significant role in increasing moisture availability and thereby creating favourable conditions for the intense precipitation observed during the event.
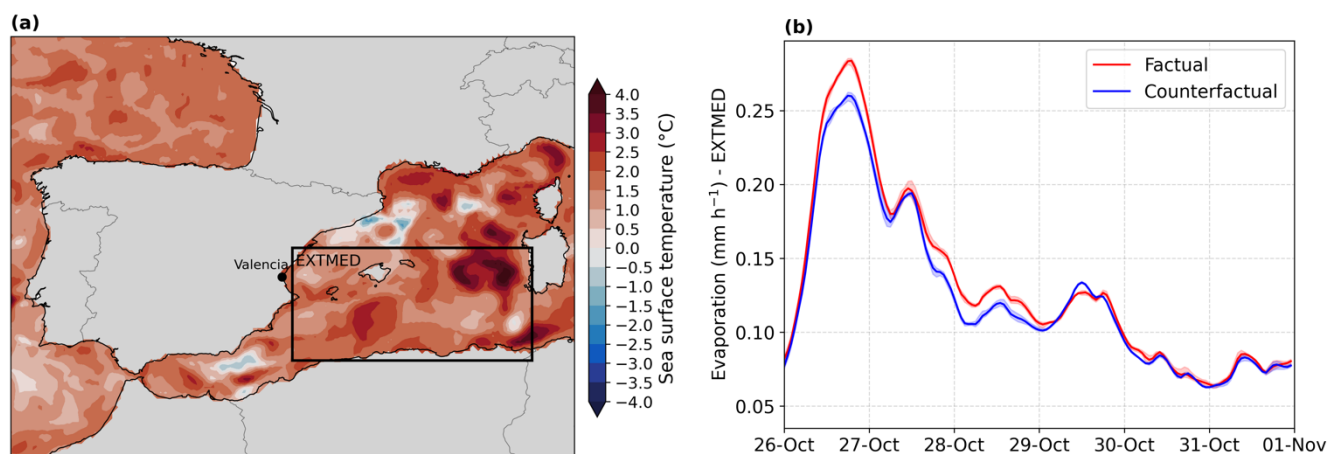
Figure 5: (a) Mean SST difference between the Factual and Counterfactual scenarios, averaged over 24-31 October. (b) Hourly evolution of evaporation (mm h-1) over the extended Mediterranean (EXTMED; box in panel a) for the Factual (red) and Counterfactual (blue) scenarios. Shading shows all the ensemble members.

3.4 Signal-to-noise ratio analysis

To strengthen the robustness of the findings presented in the previous section, we apply a signal-to-noise ratio approach to disentangle the climate change signal from internal variability. Specifically, we test whether the differences between ensemble members of the Factual and Counterfactual scenarios are statistically distinguishable from the variability observed within each scenario.

In general, the climate change signal is detectable across all variables. The intra-scenario distributions (for the Counterfactual, Count–Count, and the Factual, Fact–Fact) show median values and interquartile ranges centred around zero, whereas the inter-scenario distributions (Fact–Count) exhibit positive median values and interquartile ranges (Fig. 6). For the moisture-related variables, TCWV and IVT, the climate change signal clearly emerges from the noise, as the median and the 25th percentile of the inter-scenario distribution exceed the 75th percentile of the intra-scenario distributions in all regions (Fig. 6d-e). This separation is particularly pronounced for TCWV, where even the 5th percentile of the inter-scenario distribution lies above the 95th percentile of the intra-scenario distributions. Similar results are observed for SST, while for evaporation, the signal is less pronounced (Fig. S8 in the Supplement).
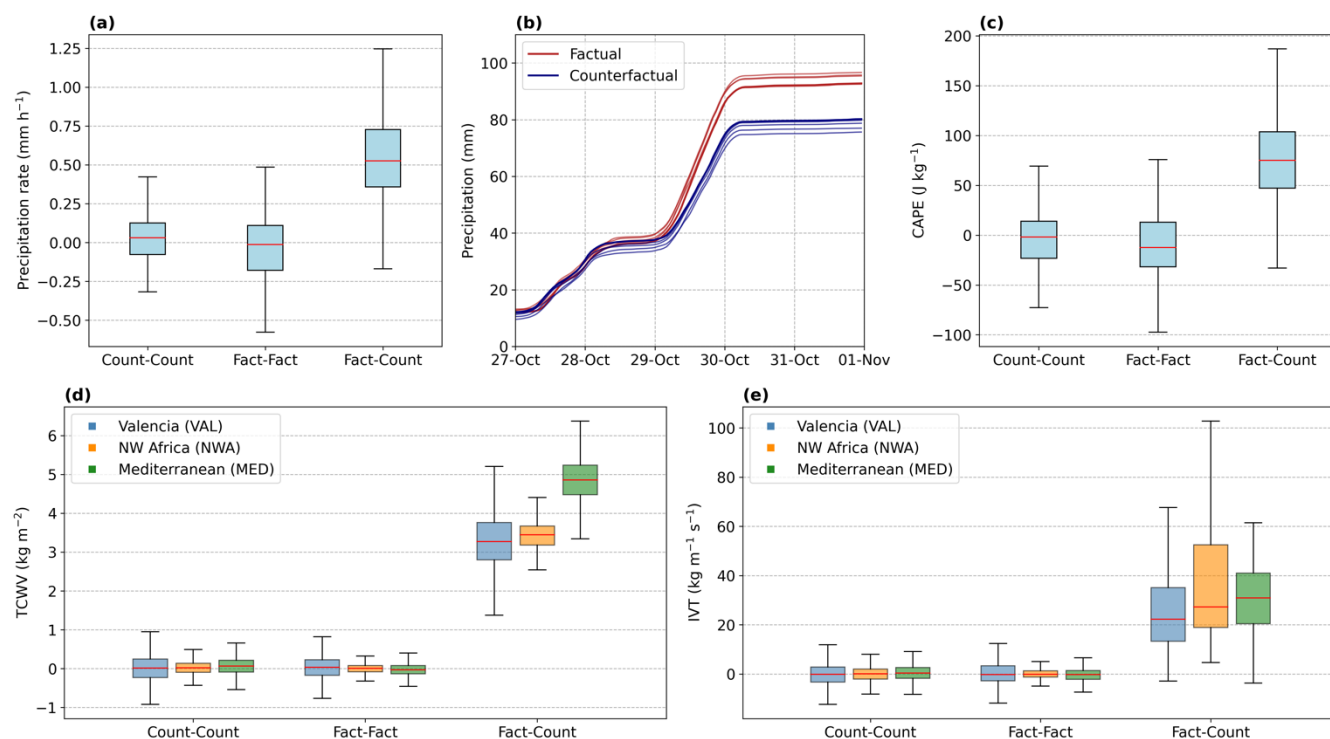
Figure 6: Distribution of hourly differences between ensemble members for the Counterfactual scenario (Count–Count), the Factual scenario (Fact–Fact), and between scenarios (Fact–Count) for (a) precipitation rate over VAL on 29 October, (c) as in (a) but for CAPE, (d) TCWV over VAL (blue), NWA (orange), and MED (green) for the 24–31 October period, and (e) as in (d) but for IVT. (b) Accumulated precipitation over VAL for ensemble members of the Factual (red) and Counterfactual (blue) scenarios. Bold lines indicate the main run. Accumulation is calculated from 24 October. The boxes show the interquartile range of the distribution (25th-75th percentiles), the red line the median (50th percentile), and the vertical bars the 5th-95th percentile range. Outliers have been removed.

For the precipitation rate, a significant climate change signal is detected on 29 October (Fig. 6a). In contrast, no clear separation between scenarios is observed for the rainfall of the preceding days. The accumulated precipitation from 24 to 28 October is indistinguishable across ensemble members of both scenarios, with totals around 40 mm. On 29 October, however, the ensemble curves start to diverge markedly, leading to a clear difference in total accumulated rainfall by the end of the period (Fig. 6b). The analysis for CAPE is similarly restricted to 29 October, as this is when the most distinct signal emerges (Fig. 6c).

These results suggest that the influence of climate change on precipitation becomes evident only beyond a certain intensity threshold. Moderate and light rainfall events remain within the range of internal variability, while heavier precipitation shows a clear positive response to the additional warming. A similar behaviour is observed outside the VAL region, particularly over southern Spain, where the exceedance probabilities between scenarios start to diverge for rates exceeding ~5 mm h-1 (Fig. S9 in the Supplement).

4 Discussion and conclusions

In late October 2024, a quasi-stationary cut-off low (COL) system affected the western Mediterranean (WMed), producing
455   intense rainfall that peaked on 29 October and caused severe impacts over Valencia, in eastern Spain. On the eastern flank of
the COL, an atmospheric-river-like (AR-like) moisture plume transported humid air from across northwestern Africa toward
the Iberian Peninsula, while additional low-level moisture originated from the warmer Mediterranean Sea. The interaction of
these moisture fluxes with the topography of the Valencia region created a highly unstable environment that favoured deep
convection and extreme rainfall. This event exemplifies the strong influence of COLs on extreme precipitation events (e.g.,
460   Nieto Ferreira, 2021; Vicente-Serrano et al., 2025) in the WMed, which are projected to become more frequent in the future
despite an overall decrease in the WMed total precipitation (Tramblay & Somot, 2018; Zittis et al., 2021) —a behaviour
often referred to as the precipitation paradox (Alpert et al., 2002; Chericoni et al., 2025).

In this study, we examined the role of climate change in enhancing the synoptic-scale environment and associated
465   precipitation over Valencia using a process-based, spectrally nudged storyline approach. This method allows for a
comparison of identical synoptic conditions under present-day (Factual) and 1950s (Counterfactual) climates, effectively
isolating the thermodynamic response while constraining large-scale dynamics. It provides a physically consistent
framework to investigate the drivers of extreme events and complements other attribution approaches within the broader
multi-method attribution community (Thompson et al., 2025).

470

From a climatological and statistical perspective, the October 2024 event was exceptional not only in terms of precipitation
over Valencia but also regarding its synoptic-scale drivers. Using long-term IFS-FESOM and ERA5 datasets, we found that
the daily precipitation, moisture transport, and instability conditions during the event exceeded the 95th percentile of their
respective climatological distributions, confirming its statistical extremeness. Both the Factual and Counterfactual scenarios
475   exceed the 95th percentile thresholds, indicating that the event would also have been classified as extreme even under the
1950s climate. This suggests that the synoptic configuration itself was sufficient to generate an extreme precipitation
episode, regardless of the background warming state.

While the synoptic configuration alone was sufficient to produce an extreme event, our results show that anthropogenic
480   warming substantially intensified its magnitude. This thermodynamic amplification is evidenced by increases of 15–25% in
both moisture content and moisture transport, particularly along the AR-like structure that channelled humid air from
northwestern Africa toward Valencia. In parallel, convective energy availability increased by about 25% over the region,
indicating enhanced atmospheric instability under present-day conditions (Fig. 7). These changes are consistent with the
Clausius-Clapeyron relationship, which predicts an increase of about 7% in atmospheric moisture per degree of warming
485   (Held & Soden, 2006). Given the ~2.2°C surface temperature difference between scenarios (based on the 8-year mean 2

meters air temperature over the 30°-60°N, 50°W-10°E domain; not shown), this corresponds to an expected moisture increase of roughly 15%, in agreement with the simulated changes. This scaling supports the thermodynamic interpretation that a warmer atmosphere can hold more water vapour, thereby enhancing the potential for extreme precipitation (O'Gorman & Muller, 2010; Schneider et al., 2010).

490
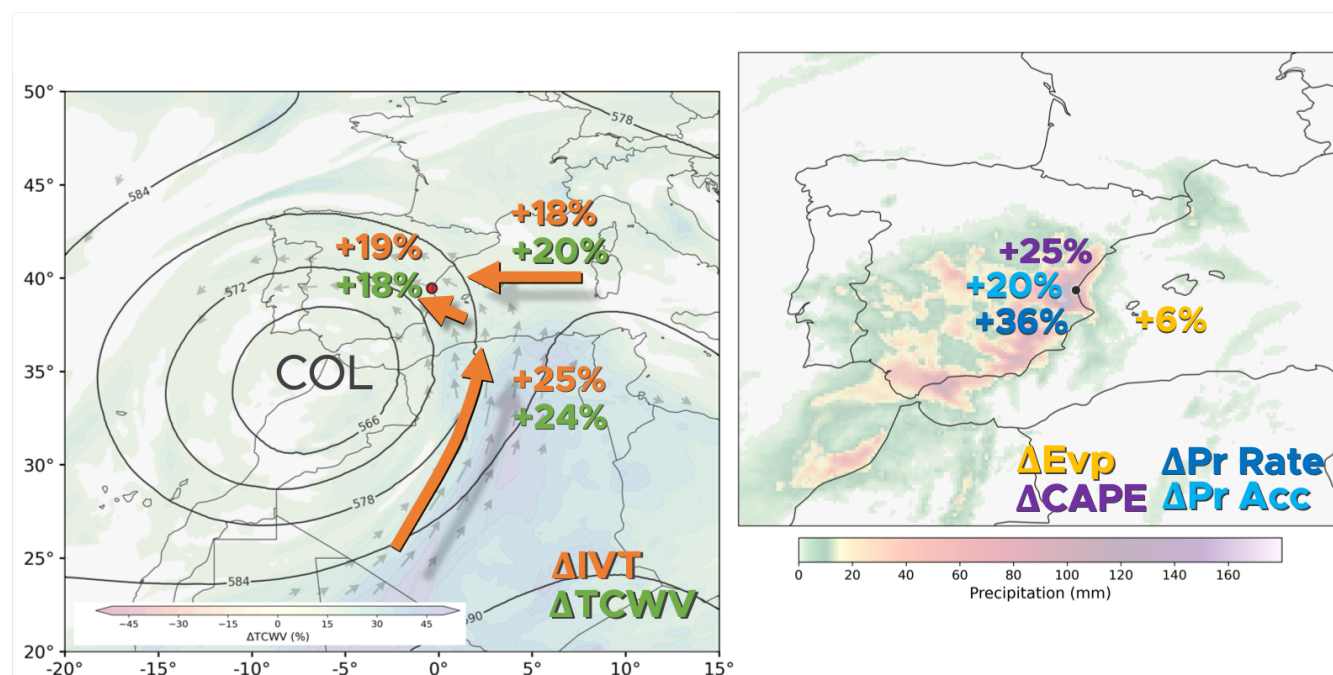
Figure 7: Schematic figure of the relative changes between Factual and Counterfactual scenarios. Total column water vapor (ΔTCWV, in green) and integrated water vapour transport (ΔIVT, in orange) on the left. Precipitation rate (ΔPr Rate, in dark blue), accumulated precipitation (ΔPr Acc, in light blue), evaporation (ΔEvp, in yellow) and convective available potential energy (ΔCAPE, in purple) on the right.

495

Under 1950 climate conditions, the same synoptic configuration would have produced approximately 20% less precipitation over the Valencia area than observed in the present-day climate (Fig. 7), consistent with previous estimates (Barriopedro et al., 2025). This apparently modest change translates into a highly non-linear response when expressed in terms of the spatial extent of extreme rainfall. For instance, considering the 90th percentile of daily precipitation in the Counterfactual scenario (142 mm), the area affected in the Valencia region doubles in the Factual scenario—from 10% to 20% of the region. For the 99th percentile (194 mm), the area experiencing such extremes increases nearly fivefold, from about 1% to almost 5%, in agreement with other recent assessments (Calvo-Sancho et al., 2025).

505

This nonlinear amplification is also evident when examining the temporal evolution of the event: the precipitation rate peaks on 29 October, coinciding with the day of maximum rainfall intensity, when precipitation rates were about 36% higher, a

value that far exceeds the scaling predicted by Clausius–Clapeyron. On the one hand, this behaviour aligns with the theoretical Clausius-Clapeyron scaling expected for temperatures below ~20 °C in the WMed, where the temperature–precipitation relationship typically follows a positive slope (Drobinski et al., 2018); on the other hand, the observed super-CC scaling is consistent with previous evidence showing that sub-daily extreme precipitation often intensifies beyond thermodynamic expectations (Formayer & Fritz, 2017; Fowler et al., 2021; Guerreiro et al., 2018). Such deviation from the theoretical CC-scaling could be partly attributed to enhanced moisture transport and convergence on 29 October, driven by the influence of an AR-like moisture structure, as reported in previous works (Lenderink et al., 2017; Prein et al., 2017), highlighting the key role of large-scale moisture fluxes in modulating precipitation intensity (Gimeno-Sotelo & Gimeno, 2023). Nevertheless, large-scale dynamics (Pfahl et al., 2017) and cloud microphysics (Calvo-Sancho et al., 2025; Fowler et al., 2021) likely also contributed to the observed amplification.

The simulations used in this study, part of the DestinE ClimateDT initiative, provide an opportunity to assess the thermodynamic response of climate change in any extreme event worldwide since 2018 (John et al., 2024). These data open the door to systematic, event-based attribution analyses at the global scale. We note, however, that the nudging applied in these simulations constrains the large-scale atmospheric circulation, limiting its ability to fully adjust to thermodynamic changes in temperature and moisture; the implications of this limitation for the attribution of extreme events should be further investigated to quantify potential under- or overestimations. The 9-km horizontal resolution also remains insufficient to fully capture the local-scale precipitation extremes observed in regions such as Valencia, where even convection-permitting regional climate models often struggle to reproduce the observed intensity and spatial variability (Calvo-Sancho et al., 2025). Finally, given the dominant role of COLs in triggering such Mediterranean extremes, future work should investigate how external drivers, such as greenhouse gases and anthropogenic aerosols, might modulate their frequency and intensity—particularly during the autumn season, when the WMed exhibits a slightly positive precipitation trend (Campos et al., 2025a).

Appendix A: Acronyms

AEMET	Spanish Meteorological Agency (Agencia Estatal de Meteorología)
AR	Atmospheric river
ASL	Above sea level
AVAMET	Valencian Meteorological Association (Associació Valenciana de Meteorologia)
CAPE	Convective available potential energy
CC	Clausius-Clapeyron

ClimateDT	Digital Twins for climate adaptation
COL	Cut-off low
DANA	Upper-level isolated depression (Depresión Aislada en Niveles Altos)
DestinE	Destination Earth
EERIE	European Eddy RIch Earth System Models
EPE	Extreme precipitation event
ERA5	ECMWF reanalysis version 5
ETCCDI	Expert team on climate change detection and indices
EXTMED	Extended Mediterranean box
FESOM	Finite volumE Sea Ice-Ocean Model
GDAS	Global Data Assimilation System
HYSPLIT	HYbrid Single Particle Lagrangian Integrated Trajectory model
IFS	Integrated Forecasting System
IVT	Integrated water vapour transport
MED	Mediterranean box
MSLP	Mean sea level pressure
MSWEP	Multi-Source Weighted-Ensemble Precipitation
NOAA	National Oceanic and Atmospheric Administration
NWA	Northwestern Africa box
OISST	Optimum Interpolation Sea Surface Temperature
Rx1day	Maximum daily precipitation index
SST	Sea surface temperature
TCWV	Total column water vapour
UTC	Universal Coordinated Time
VAL	Valencia box
WMed	Western Mediterranean

Code availability

All the Jupyter Notebooks and codes used for the analysis will be available in a GitHub repository after acceptance.

Data availability

Data from the IFS-FESOM storyline runs are available through the DestinE DESP platform https://destine-data-lake-
535 docs.data.destination-earth.eu/en/latest/introduction/introduction.html. Data from the long IFS-FESOM run is available through the World Data Center for Climate platform https://www.wdc-climate.de/ui/entry?acronym=EERIE_FESOM_hist_v1. ERA5 reanalysis and E-OBS data are accessible via the Copernicus Climate Data Store https://cds.climate.copernicus.eu/datasets. MSWEP data is accessible via the NCAR Climate Data Guide https://climatedataguide.ucar.edu/climate-data/global-high-resolution-precipitation-mswep. NOAA OISSTv2 dataset is
540 available on the NOAA Physical Sciences Laboratory webpage https://psl.noaa.gov/data/gridded/data.noaa.oisst.v2.highres.html. Daily precipitation data from AEMET is available here https://opendata.aemet.es/centrodedescargas/productosAEMET. Daily precipitation data from AVAMET are available here https://www.avamet.org/mx-meteoxarxa.php. The HYSPLIT model can be run at the NOAA Air Resources Laboratory portal https://www.ready.noaa.gov/HYSPLIT.php.

545 **Author contribution**

DC, KG and RS designed the methodology for the study. SB and AJ prepared and ran the storyline simulations. DC conducted the analyses, produced the visualisations, and wrote the paper. MO and FDR supervised. All the authors contributed to the review and editing process.

Competing interests

550 The authors declare that they have no conflict of interest.

Acknowledgements

We would like to acknowledge the European Commission Destination Earth Program and the GLORIA project funded by the Spanish MICIU/AEI and by the European Union NextGenerationEU/PRTR. We also acknowledge the EERIE project.

Financial support

555 RIS and MO are funded by the AI4Science PN070500 fellowship within the "Generación D" initiative, Red.es, Ministerio para la Transformación Digital y de la Funión Pública, for talent attraction (C005/24-ED CV1). Funded by the European Union NextGenerationEU funds, through PRTR.

References

AEMET. (2024). Estudio sobre la situación de lluvias intensas, localmente torrenciales y persistentes, en la Península Ibérica
560 y Baleares entre los días 28 de octubre y 4 de noviembre de 2024. Agencia Estatal de Meteorología.

Alpert, P., Ben-Gai, T., Baharad, A., Benjamini, Y., Yekutieli, D., Colacino, M., Diodato, L., Ramis, C., Homar, V., Romero, R., Michaelides, S., & Manes, A. (2002). The paradoxical increase of Mediterranean extreme daily rainfall in spite of decrease in total values. Geophysical Research Letters, 29(11). https://doi.org/10.1029/2001GL013554

Barrett, B. S., Campos, D. A., Veloso, J. V., & Rondanelli, R. (2016). Extreme temperature and precipitation events in
565 March 2015 in central and northern Chile. Journal of Geophysical Research: Atmospheres, 121(9), 4563–4580. https://doi.org/10.1002/2016JD024835

Barriopedro, D., Jiménez-Esteve, B., Collazo, S., Garrido-Perez, J. M., Johnson, J. E., & García-Herrera, R. (2025). A multi-method attribution analysis of the Spain's 2024 extreme precipitation event. Bulletin of the American Meteorological Society, BAMS-D-25-0049.1. https://doi.org/10.1175/BAMS-D-25-0049.1

570 Baulenas, E., Versteeg, G., Terrado, M., Mindlin, J., & Bojovic, D. (2023). Assembling the climate story: Use of storyline approaches in climate-related science. Global Challenges, 7(7), 2200183. https://doi.org/10.1002/gch2.202200183

Beck, H. E., Wood, E. F., Pan, M., Fisher, C. K., Miralles, D. G., Van Dijk, A. I. J. M., McVicar, T. R., & Adler, R. F. (2019). MSWEP V2 Global 3-Hourly 0.1° Precipitation: Methodology and Quantitative Assessment. Bulletin of the American Meteorological Society, 100(3), 473–500. https://doi.org/10.1175/BAMS-D-17-0138.1

575 Bozkurt, D., Rondanelli, R., Garreaud, R., & Arriagada, A. (2016). Impact of warmer eastern tropical Pacific SST on the March 2015 Atacama floods. Monthly Weather Review, 144(11), 4441–4460.

Calvo-Sancho, C., Díaz-Fernández, J., González-Alemán, J. J., Halifa-Marín, A., Miglietta, M., Azorin-Molina, C., Prein, A. F., Montoro-Mendoza, A., Bolgiani, P., Morata, A., & Martín, M. L. (2025). Climate change unleashed: Physical-based attribution analysis proves human-induced amplification of Valencia's deadly flooding. https://doi.org/10.21203/rs.3.rs-
580 6709965/v1

Campos, D. A., Olmo, M. E., Cos, P., Muñoz, Á. G., & Doblas-Reyes, F. J. (2025)a. Regional Aspects of Observed Temperature and Precipitation Trends in the Western Mediterranean: Insights From a Timescale Decomposition Analysis. Journal of Geophysical Research: Atmospheres, 130(19), e2024JD042637. https://doi.org/10.1029/2024JD042637

Campos, D. A., Olmo, M. E., Cos, P., Samsó, M., & Doblas-Reyes, F. (2025)b. Anthropogenic Influence on Temperature
585   and Precipitation Trends in the Western Mediterranean: A Multi-Method Approach. In Review.
       https://doi.org/10.21203/rs.3.rs-7904665/v1

Cánovas-García, F., & Vargas Molina, J. (2025). An exploration of exposure to river flood risk in Spain using the National
       Floodplain Mapping System. Geomatics, Natural Hazards and Risk, 16(1), 2421405.
       https://doi.org/10.1080/19475705.2024.2421405

590   Chericoni, M., Fosser, G., Flaounas, E., Gaetani, M., & Anav, A. (2025). Unravelling drivers of the future Mediterranean
       precipitation paradox during cyclones. Npj Climate and Atmospheric Science, 8(1), 260. https://doi.org/10.1038/s41612-
       025-01121-w

Copernicus Climate Change Service. (2018). ERA5 hourly data on pressure levels from 1940 to present [Dataset].
       Copernicus Climate Change Service (C3S) Climate Data Store (CDS). https://doi.org/10.24381/CDS.BD0915C6

595   Cornes, R. C., Van Der Schrier, G., Van Den Besselaar, E. J. M., & Jones, P. D. (2018). An Ensemble Version of the E-OBS
       Temperature and Precipitation Data Sets. Journal of Geophysical Research: Atmospheres, 123(17), 9391–9409.
       https://doi.org/10.1029/2017JD028200

Cortès, M., Llasat, M. C., Gilabert, J., Llasat-Botija, M., Turco, M., Marcos, R., Martín Vide, J. P., & Falcón, L. (2018).
       Towards a better understanding of the evolution of the flood risk in Mediterranean urban areas: The case of Barcelona.
600   Natural Hazards, 93(S1), 39–60. https://doi.org/10.1007/s11069-017-3014-0

Cos, J., Doblas-Reyes, F., Jury, M., Marcos, R., Bretonnière, P.-A., & Samsó, M. (2022). The Mediterranean climate change
       hotspot in the CMIP5 and CMIP6 projections. Earth Syst. Dynam., 13(1), 321–340. https://doi.org/10.5194/esd-13-321-2022

Danilov, S., Sidorenko, D., Wang, Q., & Jung, T. (2017). The Finite-volumE Sea ice–Ocean Model (FESOM2).
       Geoscientific Model Development, 10(2), 765–789. https://doi.org/10.5194/gmd-10-765-2017

605   Doblas-Reyes, F. J., Kontkanen, J., Sandu, I., Acosta, M., Al Turjmam, M. H., Alsina-Ferrer, I., Andrés-Martínez, M.,
       Arriola, L., Axness, M., Batlle Martín, M., Bauer, P., Becker, T., Beltrán, D., Beyer, S., Bockelmann, H., Bretonnière, P.-A.,
       Cabaniols, S., Caprioli, S., Castrillo, M., … Zimmermann, J. (2025). The Destination Earth digital twin for climate change
       adaptation. Climate and Earth system modeling. https://doi.org/10.5194/egusphere-2025-2198

Drobinski, P., Silva, N. D., Panthou, G., Bastin, S., Muller, C., Ahrens, B., Borga, M., Conte, D., Fosser, G., Giorgi, F.,
610   Güttler, I., Kotroni, V., Li, L., Morin, E., Önol, B., Quintana-Segui, P., Romera, R., & Torma, C. Z. (2018). Scaling
       precipitation extremes with temperature in the Mediterranean: Past climate assessment and projection in anthropogenic
       scenarios. Climate Dynamics, 51(3), 1237–1257. https://doi.org/10.1007/s00382-016-3083-x

ECMWF. (2023). ECMWF Newsletter 176: IFS upgrade brings many improvements and unifies medium-range resolutions.
       https://www.ecmwf.int/en/newsletter/176/earth-system-science/ifs-upgrade-brings-many-improvements-and-unifies-medium

615   Faranda, D., Alvarez-Castro, M. C., Ginesta, M., Coppola, E., & Pons, F. M. E. (2024). Heavy precipitations in October
       2024 South-Eastern Spain DANA mostly strengthened by human-driven climate change. ClimaMeter, Institut Pierre Simon
       Laplace, CNRS. https://doi.org/10.5281/ZENODO.14052041

Feser, F., & Shepherd, T. G. (2025). The concept of spectrally nudged storylines for extreme event attribution. Communications Earth & Environment, 6(1), 677. https://doi.org/10.1038/s43247-025-02659-6

620 Formayer, H., & Fritz, A. (2017). Temperature dependency of hourly precipitation intensities - surface versus cloud layer temperature: PRECIPITATION INTENSITIES: SURFACE VERSUS CLOUD LAYER TEMPERATURE. International Journal of Climatology, 37(1), 1–10. https://doi.org/10.1002/joc.4678

Fowler, H. J., Lenderink, G., Prein, A. F., Westra, S., Allan, R. P., Ban, N., Barbero, R., Berg, P., Blenkinsop, S., Do, H. X., Guerreiro, S., Haerter, J. O., Kendon, E. J., Lewis, E., Schaer, C., Sharma, A., Villarini, G., Wasko, C., & Zhang, X. (2021).

625 Anthropogenic intensification of short-duration rainfall extremes. Nature Reviews Earth & Environment, 2(2), 107–122. https://doi.org/10.1038/s43017-020-00128-6

Ghosh, R., Cheedela, S. K., Wickramage, C., Wachsmann, F., Beyer, S., Aengenheyster, M., Becker, T., Rackow, T., Koldunov, N., Sidorenko, D., & Jung, T. (2025). EERIE: Ocean Eddy-rich Kilometer-scale Climate Simulation with Integrated Forecasting System (IFS) - Finite volumE Sea Ice-Ocean Model (FESOM2.5): historical simulation (Version 1)

630 (Version 1, p. 27110209466186 Bytes) [Application/x-netcdf]. World Data Center for Climate (WDCC) at DKRZ. https://doi.org/10.26050/WDCC/EERIE_FESOM_HIST_V1

Gimeno, L., Sorí, R., Vázquez, M., Stojanovic, M., Algarra, I., Eiras-Barca, J., Gimeno-Sotelo, L., & Nieto, R. (2022). Extreme precipitation events. WIREs Water, 9(6), e1611. https://doi.org/10.1002/wat2.1611

Gimeno, L., Trigo, R. M., Ribera, P., & García, J. A. (2007). Editorial: Special issue on cut-off low systems (COL).

635 Meteorology and Atmospheric Physics, 96(1–2), 1–2. https://doi.org/10.1007/s00703-006-0216-5

Gimeno-Sotelo, L., & Gimeno, L. (2023). Where does the link between atmospheric moisture transport and extreme precipitation matter? Weather and Climate Extremes, 39, 100536. https://doi.org/10.1016/j.wace.2022.100536

Gründemann, G. J., Van De Giesen, N., Brunner, L., & Van Der Ent, R. (2022). Rarest rainfall events will see the greatest relative increase in magnitude under future climate change. Communications Earth & Environment, 3(1), 235.

640 https://doi.org/10.1038/s43247-022-00558-8

Guerreiro, S. B., Fowler, H. J., Barbero, R., Westra, S., Lenderink, G., Blenkinsop, S., Lewis, E., & Li, X.-F. (2018). Detection of continental-scale intensification of hourly rainfall extremes. Nature Climate Change, 8(9), 803–807. https://doi.org/10.1038/s41558-018-0245-3

Held, I. M., & Soden, B. J. (2006). Robust responses of the hydrological cycle to global warming. Journal of Climate,

645 19(21), 5686–5699.

Hersbach, H., Bell, B., Berrisford, P., Hirahara, S., Horányi, A., Muñoz-Sabater, J., Nicolas, J., Peubey, C., Radu, R., Schepers, D., Simmons, A., Soci, C., Abdalla, S., Abellan, X., Balsamo, G., Bechtold, P., Biavati, G., Bidlot, J., Bonavita, M., … Thépaut, J. (2020). The ERA5 global reanalysis. Quarterly Journal of the Royal Meteorological Society, 146(730), 1999–2049. https://doi.org/10.1002/qj.3803

650 Hewitt, H., Fox-Kemper, B., Pearson, B., Roberts, M., & Klocke, D. (2022). The small scales of the ocean may hold the key to surprises. Nature Climate Change, 12(6), 496–499. https://doi.org/10.1038/s41558-022-01386-6

Hoffmann, J., Bauer, P., Sandu, I., Wedi, N., Geenen, T., & Thiemert, D. (2023). Destination Earth – A digital twin in support of climate services. Climate Services, 30, 100394. https://doi.org/10.1016/j.cliser.2023.100394

Huang, B., Liu, C., Banzon, V., Freeman, E., Graham, G., Hankins, B., Smith, T., & Zhang, H.-M. (2021). Improvements of the Daily Optimum Interpolation Sea Surface Temperature (DOISST) Version 2.1. Journal of Climate, 34(8), 2923–2939. https://doi.org/10.1175/JCLI-D-20-0166.1

Insua-Costa, D., Miguez-Macho, G., & Llasat, M. C. (2019). Local and remote moisture sources for extreme precipitation: A study of the two catastrophic 1982 western Mediterranean episodes. Hydrology and Earth System Sciences, 23(9), 3885–3900. https://doi.org/10.5194/hess-23-3885-2019

IPCC. (2023). Climate Change 2021 – The Physical Science Basis: Working Group I Contribution to the Sixth Assessment Report of the Intergovernmental Panel on Climate Change (1st ed.). Cambridge University Press. https://doi.org/10.1017/9781009157896

John, A., Beyer, S., Athanase, M., Benítez, A. S., Goessling, H., Hossain, A., Nurisso, M., Aguridan, R., Andrés-Martínez, M., Gaya-Àvila, A., Cheedela, S. K., Geier, P., Ghosh, R., Hadade, I., Koldunov, N. V., Pedruzo-Bagazgoitia, X., Rackow, T., Sandu, I., Sidorenko, D., … Jung, T. (2024). Global Storyline Simulations at the Kilometre-scale. https://doi.org/10.22541/essoar.173160166.64258929/v1

Lenderink, G., Barbero, R., Loriaux, J. M., & Fowler, H. J. (2017). Super-Clausius–Clapeyron Scaling of Extreme Hourly Convective Precipitation and Its Relation to Large-Scale Atmospheric Conditions. Journal of Climate, 30(15), 6037–6052. https://doi.org/10.1175/JCLI-D-16-0808.1

Lionello, P., & Scarascia, L. (2020). The relation of climate extremes with global warming in the Mediterranean region and its north versus south contrast. Regional Environmental Change, 20(1), 31. https://doi.org/10.1007/s10113-020-01610-z

Llasat, M. C. (2024). Spain's flash floods reveal a desperate need for improved mitigation efforts. Nature, 635(8040), 787–787. https://doi.org/10.1038/d41586-024-03825-0

Martin-Moreno, J. M., Garcia-Lopez, E., Guerrero-Fernandez, M., Alfonso-Sanchez, J. L., & Barach, P. (2025). Devastating "DANA" Floods in Valencia: Insights on Resilience, Challenges, and Strategies Addressing Future Disasters. Public Health Reviews, 46, 1608297. https://doi.org/10.3389/phrs.2025.1608297

May, R. M., Goebbert, K. H., Thielen, J. E., Leeman, J. R., Camron, M. D., Bruick, Z., Bruning, E. C., Manser, R. P., Arms, S. C., & Marsh, P. T. (2022). MetPy: A Meteorological Python Library for Data Analysis and Visualization. Bulletin of the American Meteorological Society, 103(10), E2273–E2284. https://doi.org/10.1175/BAMS-D-21-0125.1

Mishra, A. N., Maraun, D., Schiemann, R., Hodges, K., Zappa, G., & Ossó, A. (2025). Long-lasting intense cut-off lows to become more frequent in the Northern Hemisphere. Communications Earth & Environment, 6(1), 115. https://doi.org/10.1038/s43247-025-02078-7

Muñoz, C., & Schultz, D. M. (2021). Cutoff Lows, Moisture Plumes, and Their Influence on Extreme-Precipitation Days in Central Chile. Journal of Applied Meteorology and Climatology, 60(4), 437–454. https://doi.org/10.1175/JAMC-D-20-0135.1

Nieto Ferreira, R. (2021). Cut-Off Lows and Extreme Precipitation in Eastern Spain: Current and Future Climate. Atmosphere, 12(7), 835. https://doi.org/10.3390/atmos12070835

Nieto, R., Sprenger, M., Wernli, H., Trigo, R. M., & Gimeno, L. (2008). Identification and Climatology of Cut-off Lows near the Tropopause. Annals of the New York Academy of Sciences, 1146(1), 256–290. https://doi.org/10.1196/annals.1446.016

O'Gorman, P. A., & Muller, C. J. (2010). How closely do changes in surface and column water vapor follow Clausius–Clapeyron scaling in climate change simulations? Environmental Research Letters, 5(2), 025207. https://doi.org/10.1088/1748-9326/5/2/025207

Olmo, M. E., Cos, P., Campos, D., Muñoz, A. G., Altava-Ortiz, V., Barrera-Escoda, A., Jury, M., Loosveldt-Tomas, S., Bretonniere, P. A., Doblas-Reyes, F., & Soret, A. (2025). Filtering CMIP6 models in the Euro-Mediterranean based on a circulation patterns approach. Weather and Climate Extremes, 100765. https://doi.org/10.1016/j.wace.2025.100765

Pall, P., Aina, T., Stone, D. A., Stott, P. A., Nozawa, T., Hilberts, A. G. J., Lohmann, D., & Allen, M. R. (2011). Anthropogenic greenhouse gas contribution to flood risk in England and Wales in autumn 2000. Nature, 470(7334), 382–385. https://doi.org/10.1038/nature09762

Pfahl, S., O'Gorman, P. A., & Fischer, E. M. (2017). Understanding the regional pattern of projected future changes in extreme precipitation. Nature Climate Change, 7(6), 423–427. https://doi.org/10.1038/nclimate3287

Porcù, F., Carrassi, A., Medaglia, C. M., Prodi, F., & Mugnai, A. (2007). A study on cut-off low vertical structure and precipitation in the Mediterranean region. Meteorology and Atmospheric Physics, 96(1–2), 121–140. https://doi.org/10.1007/s00703-006-0224-5

Prein, A. F., Rasmussen, R. M., Ikeda, K., Liu, C., Clark, M. P., & Holland, G. J. (2017). The future intensification of hourly precipitation extremes. Nature Climate Change, 7(1), 48–52. https://doi.org/10.1038/nclimate3168

Rackow, T., Pedruzo-Bagazgoitia, X., Becker, T., Milinski, S., Sandu, I., Aguridan, R., Bechtold, P., Beyer, S., Bidlot, J., Boussetta, S., Deconinck, W., Diamantakis, M., Dueben, P., Dutra, E., Forbes, R., Ghosh, R., Goessling, H. F., Hadade, I., Hegewald, J., … Ziemen, F. (2025). Multi-year simulations at kilometre scale with the Integrated Forecasting System coupled to FESOM2.5 and NEMOv3.4. Geoscientific Model Development, 18(1), 33–69. https://doi.org/10.5194/gmd-18-33-2025

Ribes, A., Thao, S., Vautard, R., Dubuisson, B., Somot, S., Colin, J., Planton, S., & Soubeyroux, J.-M. (2019). Observed increase in extreme daily rainfall in the French Mediterranean. Climate Dynamics, 52(1–2), 1095–1114. https://doi.org/10.1007/s00382-018-4179-2

Sánchez-Benítez, A., Goessling, H., Pithan, F., Semmler, T., & Jung, T. (2022). The July 2019 European Heat Wave in a Warmer Climate: Storyline Scenarios with a Coupled Model Using Spectral Nudging. Journal of Climate, 35(8), 2373–2390. https://doi.org/10.1175/JCLI-D-21-0573.1

Santer, B. D., Solomon, S., Pallotta, G., Mears, C., Po-Chedley, S., Fu, Q., Wentz, F., Zou, C.-Z., Painter, J., Cvijanovic, I., & Bonfils, C. (2017). Comparing Tropospheric Warming in Climate Models and Satellite Data. Journal of Climate, 30(1),

720   373–392. https://doi.org/10.1175/JCLI-D-16-0333.1

Saurral, R. I., Doblas-Reyes, F. J., Screen, J. A., Catto, J. L., Hay, S., & Yu, H. (2025). Western Mediterranean Droughts Fostered by Arctic Sea Ice Loss. Journal of Climate, 38(13), 3005–3014. https://doi.org/10.1175/JCLI-D-25-0066.1

Schär, C., Fuhrer, O., Arteaga, A., Ban, N., Charpilloz, C., Di Girolamo, S., Hentgen, L., Hoefler, T., Lapillonne, X., Leutwyler, D., Osterried, K., Panosetti, D., Rüdisühli, S., Schlemmer, L., Schulthess, T. C., Sprenger, M., Ubbiali, S., &

725   Wernli, H. (2020). Kilometer-Scale Climate Models: Prospects and Challenges. Bulletin of the American Meteorological Society, 101(5), E567–E587. https://doi.org/10.1175/BAMS-D-18-0167.1

Schneider, T., O'Gorman, P. A., & Levine, X. J. (2010). WATER VAPOR AND THE DYNAMICS OF CLIMATE CHANGES. Reviews of Geophysics, 48(3), RG3001. https://doi.org/10.1029/2009RG000302

Scholz, P., Sidorenko, D., Gurses, O., Danilov, S., Koldunov, N., Wang, Q., Sein, D., Smolentseva, M., Rakowsky, N., &

730   Jung, T. (2019). Assessment of the Finite-volumE Sea ice-Ocean Model (FESOM2.0) – Part 1: Description of selected key model elements and comparison to its predecessor version. Geoscientific Model Development, 12(11), 4875–4899. https://doi.org/10.5194/gmd-12-4875-2019

Shepherd, T. G., Boyd, E., Calel, R. A., Chapman, S. C., Dessai, S., Dima-West, I. M., Fowler, H. J., James, R., Maraun, D., Martius, O., Senior, C. A., Sobel, A. H., Stainforth, D. A., Tett, S. F. B., Trenberth, K. E., Van Den Hurk, B. J. J. M.,

735   Watkins, N. W., Wilby, R. L., & Zenghelis, D. A. (2018). Storylines: An alternative approach to representing uncertainty in physical aspects of climate change. Climatic Change, 151(3–4), 555–571. https://doi.org/10.1007/s10584-018-2317-9

Stein, A. F., Draxler, R. R., Rolph, G. D., Stunder, B. J. B., Cohen, M. D., & Ngan, F. (2015). NOAA's HYSPLIT Atmospheric Transport and Dispersion Modeling System. Bulletin of the American Meteorological Society, 96(12), 2059–2077. https://doi.org/10.1175/BAMS-D-14-00110.1

740   Terray, L., & Bador, M. (2025). Influence of large-scale atmospheric circulation and Mediterranean sea surface temperature to extreme land precipitation: The case of storm Alex. Environmental Research: Climate, 4(1), 015002. https://doi.org/10.1088/2752-5295/adaa0d

Thompson, V., Ermis, S., & Athanase, M. (2025). The need for multi-method extreme event attribution. Weather, wea.7779. https://doi.org/10.1002/wea.7779

745   Tramblay, Y., & Somot, S. (2018). Future evolution of extreme precipitation in the Mediterranean. Climatic Change, 151(2), 289–302. https://doi.org/10.1007/s10584-018-2300-5

Tsuji, H., & Takayabu, Y. N. (2019). Precipitation Enhancement via the Interplay between Atmospheric Rivers and Cutoff Lows. Monthly Weather Review, 147(7), 2451–2466. https://doi.org/10.1175/MWR-D-18-0358.1

Tuel, A., & Eltahir, E. A. B. (2020). Why Is the Mediterranean a Climate Change Hot Spot? JOURNAL OF CLIMATE, 33.

750   Valenzuela, R., Garreaud, R., Vergara, I., Campos, D., Viale, M., & Rondanelli, R. (2022). An extraordinary dry season precipitation event in the subtropical Andes: Drivers, impacts and predictability. Weather and Climate Extremes, 37, 100472. https://doi.org/10.1016/j.wace.2022.100472

Van Garderen, L., Feser, F., & Shepherd, T. G. (2021). A methodology for attributing the role of climate change in extreme events: A global spectrally nudged storyline. Natural Hazards and Earth System Sciences, 21(1), 171–186.
755   https://doi.org/10.5194/nhess-21-171-2021

Van Garderen, L., & Mindlin, J. (2022). A storyline attribution of the 2011/2012 drought in Southeastern South America. Weather, 77(6), 212–218. https://doi.org/10.1002/wea.4185

Vicente-Serrano, S. M., Garrido-Perez, J. M., Fernández-Álvarez, J. C., Gimeno-Sotelo, L., Beguería, S., Halifa-Marín, A., Latorre, B., El Kenawy, A. M., Franquesa, M., Adell-Michavila, M., Domínguez-Castro, F., Barriopedro, D., Gimeno-Presa,
760   L., Nieto, R., Azorin-Molina, C., Andres-Martin, M., Gutiérrez, J. M., & García-Herrera, R. (2025). Characteristics of widespread extreme precipitation events in Peninsular Spain and the Balearic Islands: Spatio-temporal dynamics and driving mechanisms. Climate Dynamics, 63(9), 340. https://doi.org/10.1007/s00382-025-07829-y

Von Storch, H., Langenberg, H., & Feser, F. (2000). A Spectral Nudging Technique for Dynamical Downscaling Purposes. Monthly Weather Review, 128(10), 3664–3673. https://doi.org/10.1175/1520-
765   0493(2000)128%253C3664:ASNTFD%253E2.0.CO;2

Wedi, N., Bauer, P., Sandu, I., Hoffmann, J., Sheridan, S., Cereceda, R., Quintino, T., Thiemert, D., & Geenen, T. (2022). Destination Earth: High-Performance Computing for Weather and Climate. Computing in Science & Engineering, 24(6), 29–37. https://doi.org/10.1109/MCSE.2023.3260519

Xiong, J., & Yang, Y. (2024). Climate Change and Hydrological Extremes. Current Climate Change Reports, 11(1), 1.
770   https://doi.org/10.1007/s40641-024-00198-4

Zhang, X., Alexander, L., Hegerl, G. C., Jones, P., Tank, A. K., Peterson, T. C., Trewin, B., & Zwiers, F. W. (2011). Indices for monitoring changes in extremes based on daily temperature and precipitation data. WIREs Climate Change, 2(6), 851–870. https://doi.org/10.1002/wcc.147

Zhuo, W., Sánchez-Benítez, A., Athanase, M., Jung, T., Yao, Y., & Goessling, H. F. (2025). Storylines reveal contrasting
775   thermodynamic effects of climate change on 2020/21 East Asian cold extremes. Npj Climate and Atmospheric Science, 8(1), 169. https://doi.org/10.1038/s41612-025-01031-x

Zittis, G., Bruggeman, A., & Lelieveld, J. (2021). Revisiting future extreme precipitation trends in the Mediterranean. Weather and Climate Extremes, 34, 100380. https://doi.org/10.1016/j.wace.2021.100380

780